

First-principles derivation of magnetic interactions in the triangular quantum spin liquid candidates KYbCh_2 ($\text{Ch} = \text{S, Se, Te}$) and AYbSe_2 ($\text{A} = \text{Na, Rb}$)

John W. Villanova^{1,*}, Allen O. Scheie², D. Alan Tennant^{3,4,5}, Satoshi Okamoto^{6,†} and Tom Berlijn^{1,‡}

¹Center for Nanophase Materials Sciences, Oak Ridge National Laboratory, Oak Ridge, Tennessee 37831, USA

²MPA-Q, Los Alamos National Laboratory, Los Alamos, New Mexico 87545, USA

³Department of Physics and Astronomy, University of Tennessee, Knoxville, Tennessee 37996, USA

⁴Department of Materials Science and Engineering, University of Tennessee, Knoxville, Tennessee 37996, USA

⁵Shull Wollan Center, Oak Ridge National Laboratory, Oak Ridge, Tennessee 37831, USA

⁶Materials Science and Technology Division, Oak Ridge National Laboratory, Oak Ridge, Tennessee 37831, USA



(Received 30 March 2023; accepted 23 June 2023; published 25 July 2023)

The AYbCh_2 ($\text{A} = \text{alkali metal}$, $\text{Ch} = \text{chalcogen}$) delafossites are a family of crystals which have a triangular lattice of effective $S = 1/2$ moments on their Yb atoms. They hold great promise for the realization of the triangular quantum spin liquid state because of their defect-minimized growth and the ability to interchange chemical constituencies among the family. Here we use *ab initio* computations to evaluate the exchange couplings of four realized (and one theoretical) rhombohedral delafossite structures and examine the influence of chemical substitution on promoting the development of a quantum spin liquid state. We find good agreement with experiment regarding the antiferromagnetic nearest-neighbor exchange J_1 , but our calculations underestimate J_2 .

DOI: [10.1103/PhysRevResearch.5.033050](https://doi.org/10.1103/PhysRevResearch.5.033050)

I. INTRODUCTION

A quantum spin liquid (QSL), broadly, is a system of interacting spins with long-range entanglement which lacks magnetic order even at zero temperature. The Lieb-Schultz-Mattis theorem guarantees that the ground state of such a system is either gapless or gapped with fractionalized topological order [1–3]. A fruitful starting place for systems which lack magnetic order is the antiferromagnetic triangular lattice which leads to highly frustrated magnetism [4]. The possibility of a resonating valence bond state on a triangular lattice with antiferromagnetically coupled nearest-neighbor spins was proposed 50 years ago [5,6], but it happens that the ground state of the Heisenberg triangular lattice antiferromagnet is the 120° Néel state [7,8]. This can be destabilized by the application of nearest-neighbor exchange anisotropy [9] or beyond-nearest-neighbor exchange [10,11].

There is growing interest in the delafossite family of materials as QSL candidates [12,13]. They are an attractive avenue for identifying a QSL state because they lack the site disorders in the nonmagnetic constituents which plague another QSL candidate, YbMgGaO_4 [14–19]. A large set of the family of delafossites AYbCh_2 ($\text{A} = \text{alkali metal}$, $\text{Ch} = \text{chalcogen}$) has been synthesized already, exhibiting antiferromagnetic coupling with a range of Curie-Weiss temperatures

and no magnetic ordering observed in the specific heat and susceptibility measurements down to 50 mK (in the $\text{A} = \text{Na}$ compounds) [20]. Neutron diffraction and measurements of the crystal electric field excitations indicate these delafossites are relatively devoid of structural disorder [11,21]. Experimental evidence of diffuse neutron spectra [12], entanglement witnesses (ruling out classical glassy states) [22], and study of the magnons of the $1/3$ -magnetization plateau at intermediate applied magnetic fields [23,24] all assist in collecting evidence of QSL features in these systems.

There is some variability of magnetic properties among the members of the delafossite family which indicates that some are more suitable QSL candidates than others. In hexagonal CsYbSe_2 , magnetic Bragg peaks start to show intensity below 400 mK [25,26]. Though magnetic ordering has been shown in KYbSe_2 below 290 mK, it is proximate to the QSL phase [22]. There has been no long-range ordering shown in RbYbSe_2 down to 400 mK [23], in KYbS_2 down to 400 mK [27], in NaYbO_2 down to 70 mK [11], in NaYbS_2 down to 50 mK [28], and in NaYbSe_2 down to 40 mK [12] and 50 mK [29,30]. Some members of this crystal family exhibit what has been called a “critical QSL” state in that they order for extremely low temperatures when a sufficiently strong (and directionally dependent) magnetic field is applied [28,29,31–35].

In AYbCh_2 the Yb atoms form a triangular lattice, and strong crystal field effects lead to the effective $S = 1/2$ Kramers doublet on each Yb site which allows for large quantum effects [36]. Additionally, each Yb-Yb bond is bisected by an inversion center, forbidding Dzyaloshinskii-Moriya interactions which would otherwise tend to temper spin frustration. [32]. It has already been stated that beyond-nearest-neighbor exchange can introduce sufficient frustration to suppress magnetic ordering; out-of-plane exchange and

*villanovajw@ornl.gov

†okapon@ornl.gov

‡berlijnt@ornl.gov

anisotropy will complicate this picture. To achieve the QSL state, the theoretical range for the ratio of the second-nearest-neighbor exchange to the nearest-neighbor exchange is $0.06 \lesssim J_2/J_1 \lesssim 0.16$ (with individual papers sometimes offering a tighter range than this) [10,37–39]. Estimates of this ratio have been given for a handful of the delafossites: CsYbSe₂, $J_2/J_1 = 0.03$ [26]; KYbSe₂, $J_2/J_1 = 0.04$ [22,24]; NaYbSe₂, $J_2/J_1 = 0.07$ [24]; and NaYbO₂, $J_2/J_1 = 0.13 - 0.15$ [11]. The AYbCh₂ family shows great promise at hosting QSL physics, but the variability even among these similar compounds underscores the need for adequate theory to buttress the search for QSLs within the delafossites.

Extensive work has been done to derive nearest-neighbor exchanges in Yb-based magnets such as pyrochlore oxides and the triangular lattice QSL candidate YbMgGaO₄ [36,40–43]. In this paper we derive the magnetic exchange couplings for KYbCh₂ ($Ch = S, Se, Te$) and AYbSe₂ ($A = Na, Rb$) for not only the nearest-neighbor bonds but also for a number of longer-range bonds. To this end, we combine density functional theory (DFT), Wannier functions, and strong-coupling perturbation theory. Our nearest-neighbor exchange couplings are in excellent agreement with experiment, but our second-nearest-neighbor exchange couplings are an order of magnitude smaller compared to experiment. We find that the exchange anisotropies are a factor of 14–69 times smaller compared to their optimal value for stabilizing a QSL. Our calculations also show there to be sizable out-of-plane interactions $J_1^{\text{out}}/J_1 \sim 0.035$.

The paper is organized as follows: In Sec. II we explain the use of DFT, Wannier functions, perturbation theory, and the model used to extract the exchange couplings. In Sec. III we analyze the hopping matrices and examine the relative magnitudes of the exchange couplings with an eye for comparison to experiment. Next we discuss the limitations and implications of the present calculation in Sec. IV, and we make our conclusions in Sec. V.

II. METHODS

We follow a three-step procedure to derive the magnetic interactions in these delafossites, following KYbSe₂ as the representative example. First we perform non-spin-polarized DFT calculations. Then we project onto Wannier functions to obtain hopping parameters and the crystal field. Finally we perform strong-coupling perturbation theory to extract the exchange parameters.

A. Density functional theory

We perform the DFT calculations as implemented in VASP [44,45]. The calculations are performed within the Perdew-Burke-Ernzerhof (PBE) generalized gradient approximation (GGA) [46] for the exchange-correlation functional with and without spin-orbit coupling (SOC). We use projector augmented wave (PAW) pseudopotentials [47,48] with an energy cutoff of 300 eV and a $9 \times 9 \times 9$ Monkhorst-Pack k -point mesh. The pseudopotential for each alkali metal and Yb treated the s and p semicore states as valence states. The energy cutoff for NaYbSe₂ is 700 eV. The experimental lattice constants for each structure are utilized, but the atomic positions are allowed to relax until component forces are

less than 1 meV/Å along each lattice vector direction in the absence of SOC.

B. Wannierization

We use WANNIER90 [49–51] to create a tight-binding Hamiltonian by projecting the band structure onto real (axial) Yb f orbitals. The maximal-localization step is not performed in order to maintain the symmetry characters of the Wannier functions. In the case without SOC the frozen window includes only the seven f bands at the Fermi level which comprise a disconnected manifold of bands; disentanglement is unnecessary. In the case with SOC the frozen window again includes those bands at the Fermi level ($[-0.3277, 0.7723]$ eV with respect to the Fermi level), but disentanglement is necessary and the disentanglement convergence criterion is set to 10^{-13} Å². The disentanglement window is $[-3.2277, 0.7723]$ eV with respect to the Fermi level. The resulting Hamiltonian is ensured to be symmetrized by postprocessing with WANNYSYMM [52], and we rotate from the axial f orbitals to the cubic f orbitals befitting our choice of coordinate system as shown in Appendix A.

C. Perturbation theory

Strong-coupling perturbation theory is used by starting with the crystal field, hopping, and SOC derived in the Wannier basis. The Hamiltonian is split into two pieces: the unperturbed part $H_0 = H_{\text{cf}} + H_{\text{soc}}^{\text{loc}} + H_{\text{int}}^{\text{loc}}$ consisting of the crystal field, local SOC, and local interacting Hamiltonian, and the perturbation $\delta H = H_{\text{hop}} + H_{\text{soc}}^{\text{nl}}$ consisting of the hopping and nonlocal SOC. H_{soc} is given by the difference, $H_{\text{rel}} - H_{\text{nrrel}}$, between the relativistic and nonrelativistic Wannier Hamiltonians, and the local part contains only the on-site parameters while the remainder comprises the nonlocal part.

Using second quantization the single-particle part of the local Hamiltonian of Yb $4f$ electrons may be expressed as

$$H_{\text{cf}} + H_{\text{soc}}^{\text{loc}} = \sum_{\sigma, \sigma'} \sum_{m, m'} h_{m, \sigma, m', \sigma} f_{m, \sigma}^{\dagger} f_{m', \sigma'}, \quad (1)$$

where $h_{m, \sigma, m', \sigma}$ includes both crystalline fields and SOC, and $f_{m, \sigma}^{\dagger}$ is an annihilation (creation) operator of an f electron with the polar component of orbital angular momentum m and spin σ .

For strongly correlated electron systems, such as Yb compounds with partially filled $4f$ orbitals, local Coulomb interactions between electrons have the largest energy scale. Local interactions for Yb $4f$ electrons may be expressed as

$$H_{\text{int}}^{\text{loc}} = \frac{1}{2} \sum_{\sigma, \sigma'} \sum_{m_1, m_2} \sum_{m'_1, m'_2} U_{m_1, m_2, m'_1, m'_2} f_{m_1, \sigma}^{\dagger} f_{m_2, \sigma'}^{\dagger} f_{m'_2, \sigma'} f_{m'_1, \sigma}. \quad (2)$$

Here, U_{m_1, m_2, m'_1, m'_2} is derived from the Coulomb integral:

$$U_{m_1, m_2, m'_1, m'_2} = \int d\mathbf{r}_1 \int d\mathbf{r}_2 \psi_{m_1}^*(\mathbf{r}_1) \psi_{m_2}^*(\mathbf{r}_2) \frac{e^2}{|\mathbf{r}_1 - \mathbf{r}_2|} \times \psi_{m'_2}(\mathbf{r}_2) \psi_{m'_1}(\mathbf{r}_1). \quad (3)$$

When electron wave functions are well approximated by atomic $4f$ orbitals, i.e., $\psi_m(\mathbf{r}) = R_{43}(r)Y_3^m(\theta, \varphi)$, this integral

is expressed using Slater integrals F^{2k} with $k \in \{0, 1, 2, 3\}$ as

$$U_{m_1, m_2, m'_1, m'_2} = \delta_{m_1+m_2, m'_1+m'_2} (-1)^{m_1-m'_1} \times \sum_{k=0}^3 c^{2k}(m_1, m'_1) c^{2k}(m_2, m'_2) F^{2k}. \quad (4)$$

Here, F^{2k} is defined by using a radial function of $4f$ orbitals, $R_{43}(r)$, as

$$F^{2k} = \int_0^\infty r_1^2 dr_1 \int_0^\infty r_2^2 dr_2 R_{43}^2(r_1) R_{43}^2(r_2) \frac{r_{>}^{2k}}{r_{<}^{2k+1}}, \quad (5)$$

where $r_{>(<)}$ is the larger (smaller) of radial coordinates r_1 and r_2 [53], and $c^{2k}(m, m')$ is defined by using spherical harmonics $Y_l^m(\theta, \varphi)$ of $4f$ orbitals as

$$c^{2k}(m, m') = \sqrt{\frac{4\pi}{4k+1}} (-1)^m \int d\Omega Y_3^{-m} Y_{2k}^{m-m'} Y_3^{m'} \\ = 7(-1)^m \begin{pmatrix} 3 & 2k & 3 \\ 0 & 0 & 0 \end{pmatrix} \begin{pmatrix} 3 & 2k & 3 \\ -m & m-m' & m' \end{pmatrix}. \quad (6)$$

The explicit dependence on the angular variables was omitted for brevity, and the parenthesized quantities are the Wigner $3j$ symbols. The values of dimensionless functions $c^{2k}(m, m')$ for f electrons are summarized in Appendix B.

The local Hamiltonian H_0 is numerically diagonalized with f -electron occupation of $n_f = 14$ for Yb^{2+} , $n_f = 13$ for Yb^{3+} , and $n_f = 12$ for Yb^{4+} . Instead of estimating each Slater integral for Yb $4f$ electrons from the first-principles calculation, we assume that the Slater integrals do not significantly depend on the valence of Yb and use experimental values as reported in Ref. [54]: $F^2 = 114\,180 \text{ cm}^{-1} = 14.156 \text{ eV}$, $F^4 = 80\,688 \text{ cm}^{-1} = 10.004 \text{ eV}$, and $F^6 = 64\,733 \text{ cm}^{-1} = 6.934 \text{ eV}$. Since F^0 for Yb systems is not known yet, we treat F_0 as a parameter and estimate exchange integrals as functions of F^0 . The dependence on F^0 is presented in Appendix C. For the specific results presented in Sec. III, we use $F^0 = 10 \text{ eV}$.

In Appendix B we show the energy spectra of the Yb ion in KYbSe_2 in two valence configurations. There is good agreement with Ref. [36], except for the degeneracy lifting of multiplets in our case because the crystalline field derived from first-principles calculations breaks the spherical symmetry.

Starting from the ground state Kramers doublet of the Yb^{3+} ion with $4f^{13}$ configuration, we carry out second-order perturbation theory calculations with respect to intersite hopping of $4f$ electrons to derive exchange interactions of intersite Yb moments.

H_0 is diagonalized exactly and δH is treated according to second-order perturbation theory,

$$\langle l | H_{\text{spin}} | l' \rangle = \sum_h \frac{\langle l | \delta H | h \rangle \langle h | \delta H | l' \rangle}{E_l - E_h}, \quad (7)$$

with E_l and $|l\rangle$ the energy and eigenstate of the degenerate low-energy state of H_0 , and E_h and $|h\rangle$ are the energies and eigenstates of the high-energy states of H_0 .

In this process it is necessary to fix the gauge of the ground state Kramers doublet or the direction of the local spin quantization axis. We first rotate the local spin axes such that the \tilde{z}

axis is normal to the Yb plane, and \tilde{x} and \tilde{y} axes are in the Yb plane. The original spin components (S^j) and the new spin components ($S^{\tilde{j}}$) represented with the new quantization axis are related via

$$\begin{pmatrix} S^x \\ S^y \\ S^z \end{pmatrix} = \frac{1}{\sqrt{6}} \begin{pmatrix} -1 & \sqrt{3} & \sqrt{2} \\ -1 & -\sqrt{3} & \sqrt{2} \\ 2 & 0 & \sqrt{2} \end{pmatrix} \begin{pmatrix} S^{\tilde{x}} \\ S^{\tilde{y}} \\ S^{\tilde{z}} \end{pmatrix}. \quad (8)$$

The ground state Kramers doublet is reexpressed so as to diagonalize the 2×2 matrix of $S^{\tilde{z}}$, and a relative phase between the doublet states is fixed appropriately. After deriving the exchange interactions in the basis with the new quantization axis, we rotate the spin axes back to the original axes.

The spin Hamiltonian is written in terms of the spin operators,

$$H_{\text{spin}} = \sum_{\gamma=x,y,z} \left(\sum_{\langle r, r' \rangle^\gamma} \mathbf{S}_r \cdot J_1^\gamma \cdot \mathbf{S}_{r'} \right) + J_1^{\text{out}} \sum_{\langle r, r' \rangle^\perp} \mathbf{S}_r \cdot \mathbf{S}_{r'} \\ + J_2 \sum_{\langle\langle r, r' \rangle\rangle} \mathbf{S}_r \cdot \mathbf{S}_{r'} + J_3 \sum_{\langle\langle\langle r, r' \rangle\rangle\rangle} \mathbf{S}_r \cdot \mathbf{S}_{r'}, \quad (9)$$

with γ ranging over the different bonds, $\langle r, r' \rangle$, $\langle\langle r, r' \rangle\rangle$, and $\langle\langle\langle r, r' \rangle\rangle\rangle$ meaning the nearest, second, and third neighbors in plane, and $\langle r, r' \rangle^\perp$ meaning the nearest out-of-plane neighbors. In particular one may inspect the nearest-neighbor exchange matrices,

$$J_1^x = \begin{pmatrix} J_1 + K_1 & \Gamma'_1 & \Gamma'_1 \\ \Gamma'_1 & J_1 & \Gamma_1 \\ \Gamma'_1 & \Gamma_1 & J_1 \end{pmatrix}, \\ J_1^y = \begin{pmatrix} J_1 & \Gamma'_1 & \Gamma_1 \\ \Gamma'_1 & J_1 + K_1 & \Gamma'_1 \\ \Gamma_1 & \Gamma'_1 & J_1 \end{pmatrix}, \quad (10) \\ J_1^z = \begin{pmatrix} J_1 & \Gamma_1 & \Gamma'_1 \\ \Gamma_1 & J_1 & \Gamma'_1 \\ \Gamma'_1 & \Gamma'_1 & J_1 + K_1 \end{pmatrix}.$$

In this study we ignore exchange anisotropies beyond the nearest in-plane neighbors due to their small numerical values. For the out-of-plane bonds we limit ourselves to the nearest neighbors for simplicity. The Dzyaloshinskii-Moriya interactions vanish due to the inversion symmetry. The m th exchange pairs are denoted in Fig. 1, and parameters of the model are reported in Tables III and IV.

D. Crystal structure

We consider the rhombohedral delafossites belonging to space group $R\bar{3}m$ (No. 166). Relevant crystallographic parameters are given in Table I and depicted in Fig. 1(a). The alkali metal, Yb , and chalcogen are at the 1b, 1a, and 2c Wyckoff sites, respectively. The Yb atoms form a triangular lattice in their layers octahedrally coordinated with chalcogen atoms, Fig. 1(b).

III. RESULTS

The electronic structure of KYbSe_2 without SOC is presented in Fig. 2(a). The Yb f bands reside at the Fermi level whereas the valence bands are comprised of Se p . The next-lowest conduction bands are primarily s character at Γ or Yb

TABLE I. Crystallographic data. The rhombohedral lattice parameter, a_r , and angle, α_r , are given in Å and degrees, respectively. x is the fractional Wyckoff coordinate and x_{rel} is the same after DFT relaxation. a_h and c_h are the hexagonal lattice parameters in Å.

	KYbS ₂ [55]	KYbSe ₂ [56]	KYbTe ₂ ^a	NaYbSe ₂ [57]	RbYbSe ₂ [23]
a_r	7.6213	7.9292	8.6578	7.3094	8.2349
α_r	30.128	30.049	30.157	32.227	29.096
x	0.2665	0.2653	–	0.2424	0.2316
x_{rel}	0.2651	0.2635	0.2640	0.2552	0.2669
a_h	3.9615	4.1110	4.5046	4.0568	4.1371
c_h	21.810	22.697	24.774	20.772	23.643

^aTheoretical structure.

d at other high-symmetry points. Application of SOC alters this picture primarily by splitting the Yb- f complex into four doubly degenerate $J = 7/2$ bands at the Fermi level and forcing three doubly degenerate $J = 5/2$ bands down into the Se p manifold (presented in Appendix D). The f -band model reproduces the bands at the Fermi level very well because of the frozen window utilized during the Wannier disentanglement process, but the lower bands are not because of their entanglement with the Se p bands. Fundamentally though, the hybridization among Yb f and Se p orbitals is taken into account in the model by demanding the bands at the Fermi level be reproduced. This can also be seen in Fig. 2(b) in the resultant Wannier functions; showing an $f_z(x^2-y^2)$ orbital as an example, the familiar f -orbital shape is present at the Yb atom and p tails exist at the Se sites both above and below the triangular lattice plane. In this regard the model contains Se- p -assisted hopping among Yb atoms beyond direct Yb-Yb exchange.

The on-site matrix elements of the model without SOC are shown in Table II. The hoppings to the nearest neighbors are presented in Appendix E. The complete set of hoppings with and without SOC is contained in the Supplemental Material [58]. The orbitals are grouped so that the symmetry afforded by the choice of the cubic-axis Cartesian system is apparent. Referring to Appendix E, within respective subblocks of the tables the hoppings associated with other

threefold partner bonds are found by cyclic permutation of $\{x, y, z\}$.

The largest hopping parameters for the nearest and second-nearest neighbors occur between the same orbital: y^3-y^3 for the X_1 bond and x^3-x^3 for the X_2 bond. However, for the third-nearest neighbor the largest hopping parameter is between different orbitals (but still within the same permuting subblock), y^3-z^3 for the X_3 bond. The largest-magnitude hopping parameter for the third-nearest neighbor even exceeds the largest hopping parameter of the second-nearest neighbor. This alerts to an issue, for previous studies fitting the inelastic neutron scattering spectrum have achieved an excellent fit on the basis of a $J_1 - J_2$ model with no recourse to J_3 [22,24].

We show the local and nonlocal SOC parameters of the model in Appendix D. As mentioned, the SOC matrix of the model is the difference between the relativistic and nonrelativistic Hamiltonians, $H_{\text{rel}} - H_{\text{nrrel}}$. In Appendix D, it is apparent that the SOC is close to the atomiclike case (there is some deviation, discussed therein). Our fitted $\lambda = 0.390$ eV is in excellent agreement with the literature for the Yb⁴⁺ ion (0.378 eV [59] and 0.380 eV [54]). However, the largest nonlocal SOC matrix element is $\sim 18\%$ of the smallest local SOC interorbital matrix element and this is not entirely negligible. This is a feature of the Yb f and Se p hybridization.

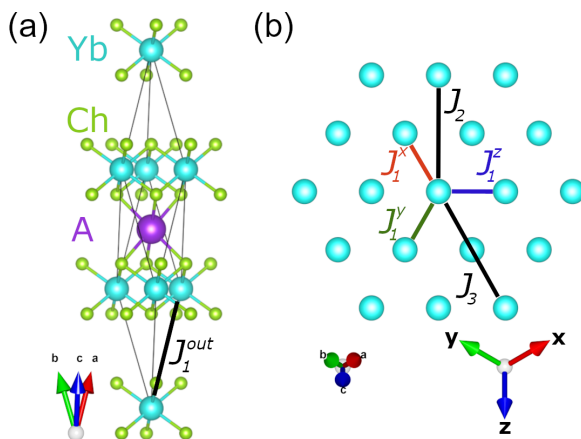


FIG. 1. Crystal structure of $AYbCh_2$. (a) The primitive cell for space group $R\bar{3}m$. The Yb atom is placed at the origin which is an inversion center. (b) The structure in plane exhibiting the triangular lattice of Yb atoms. The symmetric choice of the Cartesian axes lying most closely along the Yb- Ch bonds is emphasized.

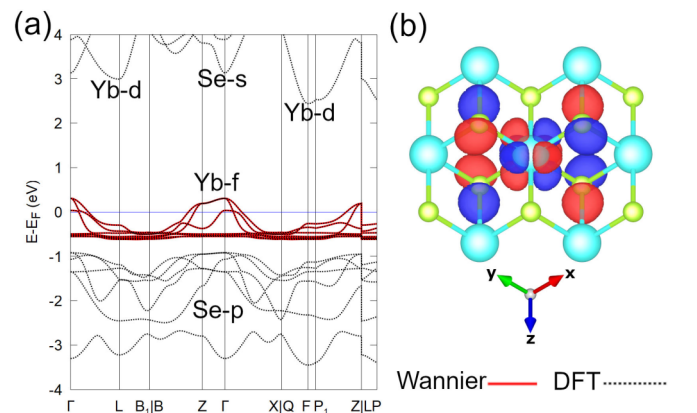


FIG. 2. (a) Band structure of $KYbSe_2$ without spin-orbit coupling. Black dashed lines are DFT and red lines are produced from WANNIER90. (b) An example of the resultant Wannier functions, here for the $f_z(x^2-y^2)$ projection. Positive (negative) isosurfaces are drawn in red (blue).

TABLE II. On-site energies (meV) without spin-orbit coupling.

	xyz	On site					
		x^3	y^3	z^3	$x(y^2-z^2)$	$y(z^2-x^2)$	$z(x^2-y^2)$
xyz	0	3.19	3.19	3.19	0	0	0
x^3	3.19	43.97	10.89	10.89	0	2.26	-2.26
y^3	3.19	10.89	43.97	10.89	-2.26	0	2.26
z^3	3.19	10.89	10.89	43.97	2.26	-2.26	0
$x(y^2-z^2)$	0	0	-2.26	2.26	-38.72	2.59	2.59
$y(z^2-x^2)$	0	2.26	0	-2.26	2.59	-38.72	2.59
$z(x^2-y^2)$	0	-2.26	2.26	0	2.59	2.59	-38.72

Table III shows the resultant exchange parameters for the model including full SOC and $F^0 = 10$ eV. For the general dependence on F^0 see Appendix C. For KYbSe₂, J_1 is more than two orders of magnitude greater than $J_2 \sim J_3$. Consistent with the examination of the hopping parameters, J_3 is even larger than J_2 . The out-of-plane exchange, J_1^{out} , is rather larger than J_2 but at least has a constant sign across the investigated materials. This is in contrast to J_2 which is antiferromagnetic except for KYbS₂ and NaYbSe₂. The signs of K_1 , Γ_1 , and Γ'_1 are constant across the materials except in the case of Γ'_1 for KYbS₂. The ratio $|J_2/J_1|$ strictly grows with substitution of heavier chalcogen atoms, and separately, strictly grows with substitution of heavier alkali metal atoms. However, due to the smallness of J_2 in the theory, $|J_2/J_1|$ is woefully small and far from the range which is conducive for a QSL.

One may also take the exchange coupling set $\{J_1, K_1, \Gamma_1, \Gamma'_1\}$ and transform to an alternative coordinate system which explicitly separates the bond-dependent anisotropic part of the Hamiltonian, described by the set $\{J, \Delta, J_{\pm\pm}, J_{z\pm}\}$ [60]. In that case Δ characterizes the easy-plane ($\Delta < 1$) or easy-axis ($\Delta > 1$) anisotropy, $J_{\pm\pm}$ the in-plane anisotropy, and $J_{z\pm}$ the off-diagonal anisotropy [61]. Across these materials $J_{\pm\pm}/J$ is tiny, which is often assumed to be the case, and is between a factor of 17 and 83 times smaller than the optimal value for a QSL [9]. That is not

TABLE III. Exchange constants. The transformed exchange constants $\{J, \Delta/J, J_{z\pm}/J, J_{\pm\pm}/J\}$ are also reported to ease comparison across the literature, including Ref. [9].

	KYbS ₂	KYbSe ₂	KYbTe ₂ ^a	NaYbSe ₂	RbYbSe ₂
J_1 (meV)	0.964	0.461	0.437	0.539	0.466
J_2 (μ eV)	-0.035	1.958	3.017	-0.505	3.288
J_3 (μ eV)	1.209	3.882	0.385	2.796	5.424
J_1^{out} (meV)	0.007	0.016	0.020	0.041	0.009
J_2/J_1	-4×10^{-5}	0.004	0.007	-0.001	0.007
J_1^{out}/J_1	0.008	0.035	0.045	0.076	0.019
K_1 (μ eV)	4.964	16.604	14.007	19.157	16.484
Γ_1 (μ eV)	-2.639	-13.659	-7.543	-10.188	-12.780
Γ'_1 (μ eV)	2.903	-3.677	-6.583	-3.252	-3.234
J (meV)	0.965	0.474	0.449	0.551	0.478
Δ/J	1.003	0.956	0.954	0.970	0.959
$J_{z\pm}/J$	-0.005	-0.026	-0.016	-0.022	-0.026
$J_{\pm\pm}/J$	0.001	0.001	-0.004	-0.002	0.001

^aTheoretical structure.TABLE IV. Exchange energies (meV) for nearest neighbor (1NN) and second-nearest neighbor (2NN) in plane and out of plane for KYbSe₂.

KYbSe ₂	$\frac{1}{2U} \sum_{ij} t_{ij} ^2$	J^a
1NN in plane	2.387	0.461
2NN in plane	0.173	0.002
1NN out of plane	0.018	0.016
2NN in plane / 1NN in plane	0.072	0.004
1NN out of plane / 1NN in plane	0.008	0.035

^aThe relevant entry appears in the upper half of Table III.

necessarily lethal for the QSL phase on its own since $J_{z\pm}/J$ is primarily dispositive of the QSL phase reported in Ref. [9]. But $J_{z\pm}/J$ across these materials is between a factor of 14 and 69 times smaller than the optimal value.

The trend for J_1 is in excellent agreement with experiments. For KYbSe₂, $J_1 = 0.463$ meV (nonlinear spin wave fit 0.456 ± 0.013 meV [24]), and for NaYbSe₂, $J_1 = 0.543$ meV (nonlinear spin wave fit 0.551 ± 0.010 meV [24]). However, the calculated J_2 is an order of magnitude too small. The ferromagnetic J_2 for NaYbSe₂ notably disagrees with experiment which indicates an antiferromagnetic J_2 [24]. The alkali metal substitutional trend for $|J_2/J_1|$ is the reverse of what has been found experimentally [24,26].

How is it that the theory so substantially underestimates J_2 ? Dissecting the different exchange paths is a complex endeavor beyond the scope of this work. Still we can glean some understanding of the smallness of J_2 by comparing the exchange couplings to the sum of the squares of the hopping parameters divided by U . This quantity serves as a rudimentary estimate of the exchange coupling which does not allow for exchange path cancellation and is reported in Table IV. The sum of the squares of the hoppings is quite comparable to the nearest-neighbor out-of-plane exchange parameter, but for the nearest and second-nearest in-plane bonds it is one and two orders of magnitude larger, respectively. This indicates that there are large cancellations occurring among the ferromagnetic and antiferromagnetic exchange paths for the second-nearest neighbors in particular. If one focuses on the ratios of these sums of squares of the hopping parameters, it is intriguing that the ratio between the second-nearest- and nearest-neighbor in-plane bonds is much closer to experiment [24] and falls into the range which is favorable for QSL development.

IV. DISCUSSION

The theory accurately captures J_1 for the two available experimental observations, but J_2 is an order of magnitude smaller compared to experiment and displays the wrong trend for alkali metal substitution. Also J_2 has the wrong sign for NaYbSe₂ compared to experiment. In our theory we included the Yb f degrees of freedom only. However, the Hubbard U is on the order of 10 eV, which is rather larger than the energy difference between the Se p and Yb f bands (i.e., charge transfer gap without SOC) that can be roughly estimated from Fig. 2 to be ~ 2 eV. Even without the Hubbard U , the SOC already pushes the Yb f bands into the Se p band complex (see Appendix D). Therefore including the

Se p degrees of freedom in the perturbation theory has the potential to improve the theoretical results compared to the experiment.

We remind the reader that the Yb f Wannier functions encode information about the Se p tails [Fig. 2(b)] which mediate the exchange and contribute to both J_1 and J_2 . Still, suppose that J_1 were dominated by direct exchange among the Yb atoms. If one were to include the Se p degrees of freedom explicitly under this assumption and compare to our result, one would find that J_1 is relatively insensitive whereas J_2 could increase with the addition of extra exchange paths. In this way it is possible (though not guaranteed) that J_2/J_1 could be enhanced when projecting onto both Yb f and Se p orbitals.

In Ref. [36] the nearest-neighbor exchange couplings were computed by including the anion p degrees of freedom and applying fourth-order perturbation theory. However, second-nearest-neighbor Yb atoms do not share a Se atom, so sixth-order perturbation theory would be necessary. Another option would be to fit the exchange couplings against total energies of various magnetic configurations obtained from DFT + U . The advantage of this approach is that it takes all degrees of freedom into account, not only Yb f and Se p but also, for example, Yb d and Se s in the conduction band [Fig. 1(a)]. The disadvantage of the total energy approach is that because of the large interactions, the exchange couplings in the transition-metal f systems are on the order of meV which is also reaching the limit of accuracy of DFT. Further, in DFT + U calculations one can easily descend into a local minimum during the self-consistent minimization, which makes the total energy approach challenging.

Since the exchange couplings in f systems are so small, dipolar interactions can possibly play a role. Using the formula from Ref. [36] we find the dipolar interaction strength for the second-nearest neighbor to be 0.0025 meV. This is comparable to the superexchanges computed in this work, but it is still an order of magnitude smaller than the experimental observations. Including dipolar interactions therefore does not account for the theoretically diminished J_2 as compared to experiment.

Our first-principles treatment allows for comprehensive inclusion of the crystalline electric field and SOC, implying a breakdown of the SU(2) symmetry. Biquadratic terms [$\sim(\mathbf{S}_r \cdot \mathbf{S}_r)^2$] are therefore permitted to arise [62], and this has been shown to be important in (especially) one- and two-dimensional systems with $S > 1/2$ [63–65]. However, since the ratio of the biquadratic-to-bilinear exchange goes as $\sim t^2/U^2$ [66], we estimate that such terms would be four orders of magnitude smaller than the nearest-neighbor exchange. We also point out that biquadratic terms were not needed to fit inelastic neutron scattering experiments on KYbSe₂ and NaYbSe₂ [22,24].

Finally it is interesting to emphasize that the nearest-neighbor out-of-plane exchange parameters are rather large. Experimentally these exchanges still need to be resolved. If indeed the out-of-plane couplings are large, then this would pose a challenge for realizing the QSL. Perhaps chemical intercalation or tensile strain could be used to increase the distance between the Yb planes and avoid this undesirable effect.

V. CONCLUSION

We have derived the magnetic exchange couplings for KYbCh₂ ($Ch = S, Se, Te$) and AYbSe₂ ($A = Na, Rb$) from first principles by combining DFT, Wannier functions, and strong-coupling perturbation theory. We found good agreement with experiment for the nearest-neighbor coupling J_1 , as well as producing as much of the chemical trend in the literature. However, when one goes to the second-nearest-neighbor exchange couplings, the theory is wanting. Our $|J_2/J_1|$ ratios are an order of magnitude smaller than those found in experiment, and the sign of J_2 for NaYbSe₂ is incorrectly ferromagnetic. The theoretical trend of the magnitude of J_2 with heavier alkali metal substitution is the reverse of the experimental trend, but our theory predicts that heavier chalcogen substitution pushes $|J_2/J_1|$ closer to the desired ratio for the QSL state. The interaction parameters indicate all of these delafossites are far from the exchange-anisotropy-induced QSL regime. We also found significant out-of-plane couplings (relative to the in-plane J_2), and it will be interesting to see how well theory compares to future experiments.

ACKNOWLEDGMENTS

This work was supported by the U.S. Department of Energy, Office of Science, National Quantum Information Science Research Centers, Quantum Science Center. This research used resources of the Compute and Data Environment for Science (CADES) at the Oak Ridge National Laboratory, which is supported by the Office of Science of the U.S. Department of Energy under Contract No. DE-AC05-00OR22725. This research also used resources of the National Energy Research Scientific Computing Center (NERSC), a U.S. Department of Energy Office of Science User Facility operated under Contract No. DE-AC02-05CH11231.

APPENDIX A: DEFINITION OF AXIAL AND CUBIC f ORBITALS

The order of the real *axial* f -orbital angular functions in WANNIER90 is

$$\begin{aligned}
 f_{z^3} &= \sqrt{\frac{7}{16\pi}} \frac{5z^3 - 3zr^2}{r^3} = Y_3^0, \\
 f_{xz^2} &= \sqrt{\frac{21}{32\pi}} \frac{x(5z^2 - r^2)}{r^3} = \frac{1}{\sqrt{2}}(Y_3^{-1} - Y_3^1), \\
 f_{yz^2} &= \sqrt{\frac{21}{32\pi}} \frac{y(5z^2 - r^2)}{r^3} = \frac{i}{\sqrt{2}}(Y_3^{-1} + Y_3^1), \\
 f_{z(x^2-y^2)} &= \sqrt{\frac{105}{16\pi}} \frac{z(x^2 - y^2)}{r^3} = \frac{1}{\sqrt{2}}(Y_3^{-2} + Y_3^2), \\
 f_{xyz} &= \sqrt{\frac{105}{16\pi}} \frac{2xyz}{r^3} = \frac{i}{\sqrt{2}}(Y_3^{-2} - Y_3^2), \\
 f_{x(x^2-3y^2)} &= \sqrt{\frac{35}{32\pi}} \frac{x(x^2 - 3y^2)}{r^3} = \frac{1}{\sqrt{2}}(Y_3^{-3} - Y_3^3), \\
 f_{y(3x^2-y^2)} &= \sqrt{\frac{35}{32\pi}} \frac{y(3x^2 - y^2)}{r^3} = \frac{i}{\sqrt{2}}(Y_3^{-3} + Y_3^3),
 \end{aligned}$$

where each is also identified as the linear combination of spherical harmonics (Y_l^m). An alternative set of angular functions is the set of real *cubic* harmonics, which is more convenient to take advantage of the symmetry of our choice of cubic Cartesian coordinate system,

$$\tilde{f}_{xyz} = \sqrt{\frac{105}{16\pi}} \frac{2xyz}{r^3} = f_{xyz},$$

$$\tilde{f}_{x^3} = \sqrt{\frac{7}{16\pi}} \frac{x(5x^2-3r^2)}{r^3} = -\sqrt{\frac{3}{8}}f_{xz^2} + \sqrt{\frac{5}{8}}f_{x(x^2-3y^2)},$$

$$\tilde{f}_{y^3} = \sqrt{\frac{7}{16\pi}} \frac{y(5y^2-3r^2)}{r^3} = -\sqrt{\frac{3}{8}}f_{yz^2} - \sqrt{\frac{5}{8}}f_{y(3x^2-y^2)},$$

$$\tilde{f}_{z^3} = \sqrt{\frac{7}{16\pi}} \frac{z(5z^2-3r^2)}{r^3} = f_{z^3},$$

$$\tilde{f}_{x(y^2-z^2)} = \sqrt{\frac{105}{16\pi}} \frac{x(y^2-z^2)}{r^3} = -\sqrt{\frac{5}{8}}f_{xz^2} - \sqrt{\frac{3}{8}}f_{x(x^2-3y^2)},$$

$$\tilde{f}_{y(z^2-x^2)} = \sqrt{\frac{105}{16\pi}} \frac{y(z^2-x^2)}{r^3} = \sqrt{\frac{5}{8}}f_{yz^2} - \sqrt{\frac{3}{8}}f_{y(3x^2-y^2)},$$

$$\tilde{f}_{z(x^2-y^2)} = \sqrt{\frac{105}{16\pi}} \frac{z(x^2-y^2)}{r^3} = f_{z(x^2-y^2)}.$$

APPENDIX B: ENERGY SPECTRUM

For Yb compounds, the crystalline field effect deduced by our first-principles calculation is found to be rather small. We show in Fig. 3 energy spectra of the Yb ion in KYbSe₂.

The Yb³⁺ ion has seven Kramers doublets: four low-energy doublets (three high-energy doublets) spread in energy by about 0.04 (0.05) eV. In the Yb⁴⁺ ion, eigenstates are clustered in 13 energy regimes with the number of states given by 13, 9, 11, 9, 7, 5, 9, 5, 13, 1, 3, 5, and 1 from low energy to high energy. The spread in energy of each cluster is at most 0.1 eV. Thus the energy scale of the crystalline field is no more than 0.1 eV, which is slightly smaller than the energy scale of SOC, and two orders of magnitude smaller than the energy scale of the Coulomb interaction.

When the crystalline field is artificially turned off, each cluster of eigenstates recovers degeneracy: for a free Yb³⁺ ion there is an eightfold-degenerate state for the lower energy states and a sixfold-degenerate state for the higher energy states (total angular momentum $\frac{7}{2}$ and $\frac{5}{2}$, respectively), and for a free Yb⁴⁺ ion, the number of degeneracy corresponds to the number of states reported for each cluster, above. The values of dimensionless functions $c^{2k}(m, m')$ for f electrons used to express the Coulomb integral in terms of Slater integrals are summarized in Table V.

APPENDIX C: EXCHANGE PARAMETER DEPENDENCE ON F^0

We present exchange parameters obtained for KYbSe₂ as functions of F^0 . As expected, exchange parameters are roughly proportional to $1/F^0$ as shown in Figs. 4(a)–4(d), but different parameters have different slopes because these are

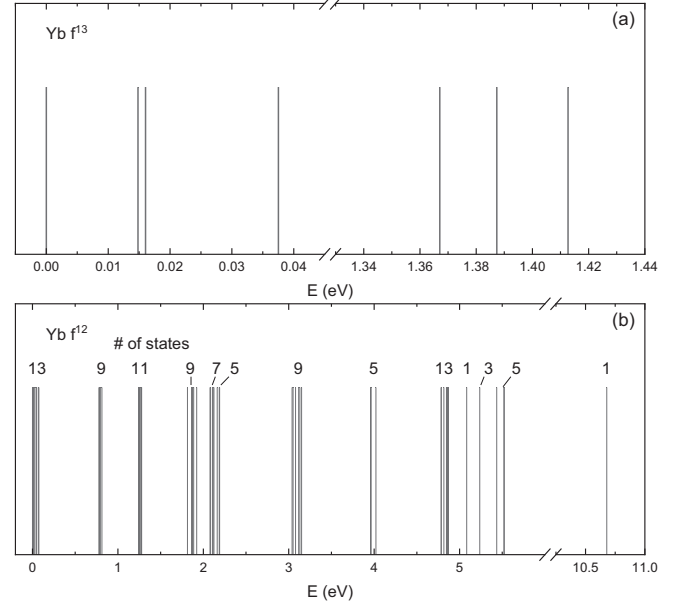


FIG. 3. Energy spectrum of Yb ion in KYbSe₂. (a) Spectrum with the $4f^{13}$ configuration for Yb³⁺, and (b) spectrum with the $4f^{12}$ configuration for Yb⁴⁺. The single-particle parameters are derived from first-principles calculations while the values of Slater integrals $F^{2,4,6}$ are taken from Ref. [54]. These results are independent of F^0 because energy is measured from the ground state of each $4f$ occupation. In (a), every energy level has Kramers degeneracy, i.e., twofold degeneracy. Numbers in (b) indicate the number of states in multiplets, whose degeneracy is lifted because the crystalline field derived from first-principles calculations for KYbSe₂ breaks the spherical symmetry.

characterized by different virtual hopping processes, exciting electrons to high-energy states in different ways.

APPENDIX D: SPIN-ORBIT COUPLING

The SOC matrix has the form

$$H_{\text{soc}} = \begin{pmatrix} h_{\uparrow\uparrow} & h_{\uparrow\downarrow} \\ -h_{\uparrow\downarrow}^* & h_{\uparrow\uparrow}^* \end{pmatrix}. \quad (\text{D1})$$

We present the topmost 7×7 blocks, and the rest of the Hamiltonian may be swiftly derived from there. For localized spherically symmetric f orbitals $H_{\text{soc}}^{\text{loc}}$ is given by $\lambda \vec{L} \cdot \vec{S}$ of the form shown in Table VI. Tables VII and VIII show the local and nonlocal SOC matrices of the model, respectively. $H_{\text{soc}}^{\text{loc}}$ is not identically of the form as the atomic SOC, e.g., the ratio of $\langle x(y^2-z^2) | \vec{L} \cdot \vec{S} | y^3 \rangle$ to $\langle y^3 | \vec{L} \cdot \vec{S} | x^3 \rangle$ is 1.49 rather than $\sqrt{15}/3$, and there are nonzero terms on the diagonal. Still, the nonlocal part is not so large and the local deviation is manageable, so we fit λ by minimizing the sum of the squared residuals for all the elements of $H_{\text{soc}}^{\text{loc}}$ against $\lambda \vec{L} \cdot \vec{S}$. There is excellent agreement between our fit, $\lambda = 0.390$ eV, and the literature for the Yb⁴⁺ ion (0.378 eV [59] and 0.380 eV [54]). The band structure of KYbSe₂ with SOC is presented in Fig. 5.

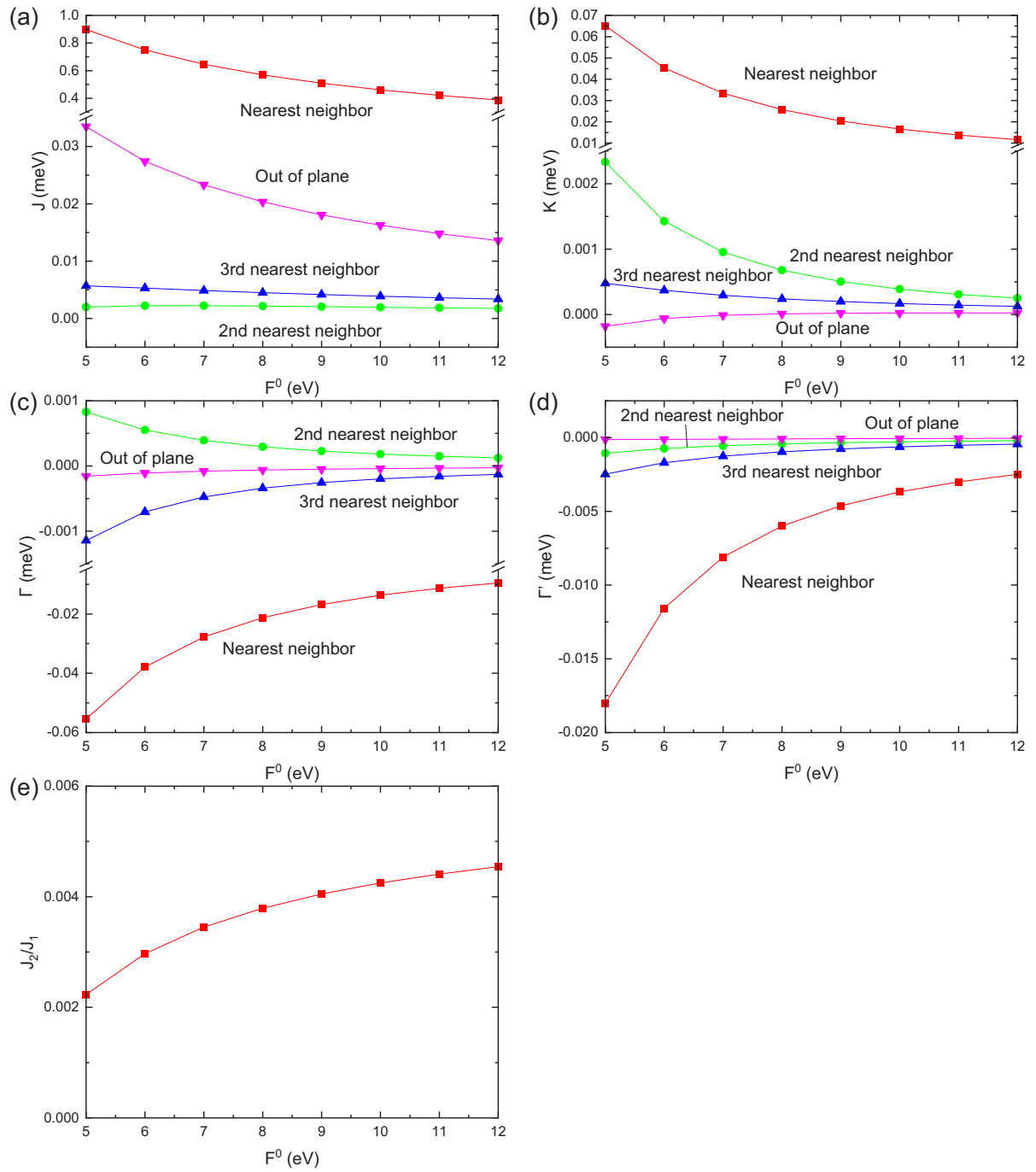


FIG. 4. Exchange parameters of KYbSe₂ as functions of F_0 . (a) Symmetric Heisenberg, (b) pseudodipolar Kitaev, (c) symmetric off-diagonal Γ , and (d) symmetric off-diagonal Γ' . (e) Ratio of second-nearest-neighbor J_2 to nearest-neighbor J_1 .

TABLE V. Values of dimensionless function $c^{2k}(m, m')$ for $l=3$. Other values can be discerned via the identity $c^{2k}(m, m') = (-1)^{m-m'} c^{2k}(m', m)$.

m	m'	c^0	$15c^2$	$33c^4$	$429c^6$
± 3	± 3	1	-5	3	-5
± 3	± 2	0	5	$-\sqrt{30}$	$5\sqrt{7}$
± 3	± 1	0	$-\sqrt{10}$	$3\sqrt{6}$	$-10\sqrt{7}$
± 3	0	0	0	$-3\sqrt{7}$	$10\sqrt{21}$
± 2	± 2	1	0	-7	30
± 2	± 1	0	$\sqrt{15}$	$4\sqrt{2}$	$-5\sqrt{105}$
± 2	0	0	$-2\sqrt{5}$	$-\sqrt{3}$	$20\sqrt{14}$
± 1	± 1	1	3	1	-75
± 1	0	0	$\sqrt{2}$	$\sqrt{15}$	$25\sqrt{14}$
0	0	1	4	6	100
± 3	∓ 3	0	0	0	$-10\sqrt{231}$
± 3	∓ 2	0	0	0	$5\sqrt{462}$
± 3	∓ 1	0	0	$\sqrt{42}$	$-5\sqrt{210}$
± 2	∓ 2	0	0	$\sqrt{70}$	$30\sqrt{14}$
± 2	∓ 1	0	0	$-\sqrt{14}$	$-15\sqrt{42}$
± 1	∓ 1	0	$-2\sqrt{6}$	$-2\sqrt{10}$	$-10\sqrt{105}$

TABLE VI. Atomic spin-orbit-coupling matrix assuming spherically symmetric localized f orbitals. This is consistent with Ref. [67] in structure, though the reference contains a matrix for the f orbitals which should be multiplied by 2.

$h_{\uparrow\uparrow}$	$\vec{L} \cdot \vec{S}$ Local						
	xyz	x^3	y^3	z^3	$x(y^2-z^2)$	$y(z^2-x^2)$	$z(x^2-y^2)$
xyz	0	0	0	0	0	0	i
x^3	0	0	$\frac{3i}{4}$	0	0	$\frac{i\sqrt{15}}{4}$	0
y^3	0	$-\frac{3i}{4}$	0	0	$\frac{i\sqrt{15}}{4}$	0	0
z^3	0	0	0	0	0	0	0
$x(y^2-z^2)$	0	0	$-\frac{i\sqrt{15}}{4}$	0	0	$-\frac{i}{4}$	0
$y(z^2-x^2)$	0	$-\frac{i\sqrt{15}}{4}$	0	0	$\frac{i}{4}$	0	0
$z(x^2-y^2)$	$-i$	0	0	0	0	0	0
$h_{\uparrow\downarrow}$	$\vec{L} \cdot \vec{S}$ Local						
	xyz	x^3	y^3	z^3	$x(y^2-z^2)$	$y(z^2-x^2)$	$z(x^2-y^2)$
xyz	0	0	0	0	i	1	0
x^3	0	0	0	$-\frac{3}{4}$	0	0	$\frac{\sqrt{15}}{4}$
y^3	0	0	0	$\frac{3i}{4}$	0	0	$\frac{i\sqrt{15}}{4}$
z^3	0	$\frac{3}{4}$	$-\frac{3i}{4}$	0	$\frac{\sqrt{15}}{4}$	$\frac{i\sqrt{15}}{4}$	0
$x(y^2-z^2)$	$-i$	0	0	$-\frac{\sqrt{15}}{4}$	0	0	$\frac{1}{4}$
$y(z^2-x^2)$	-1	0	0	$-\frac{i\sqrt{15}}{4}$	0	0	$-\frac{i}{4}$
$z(x^2-y^2)$	0	$-\frac{\sqrt{15}}{4}$	$-\frac{i\sqrt{15}}{4}$	0	$-\frac{1}{4}$	$\frac{i}{4}$	0

TABLE VII. Spin-orbit coupling parameters (meV) for the local part of the Hamiltonian, $H_{\text{soc}}^{\text{loc}}$. Only elements greater than or equal to 10 meV are shown.

$h_{\uparrow\uparrow}$	Local						
	xyz	x^3	y^3	z^3	$x(y^2-z^2)$	$y(z^2-x^2)$	$z(x^2-y^2)$
xyz	0	0	0	0	0	0	$392i$
x^3	0	42	$262i$	0	0	$390i$	0
y^3	0	$-262i$	42	0	$390i$	0	0
z^3	0	0	0	42	0	0	0
$x(y^2-z^2)$	0	0	$-390i$	0	-11	$-80i$	0
$y(z^2-x^2)$	0	$-390i$	0	0	$80i$	-11	0
$z(x^2-y^2)$	$-392i$	0	0	0	0	0	-11
$h_{\uparrow\downarrow}$	Local						
	xyz	x^3	y^3	z^3	$x(y^2-z^2)$	$y(z^2-x^2)$	$z(x^2-y^2)$
xyz	0	0	0	0	$392i$	392	0
x^3	0	0	0	-262	0	0	390
y^3	0	0	0	$262i$	0	0	$390i$
z^3	0	262	$-262i$	0	390	$390i$	0
$x(y^2-z^2)$	$-392i$	0	0	-390	0	0	80
$y(z^2-x^2)$	-392	0	0	$-390i$	0	0	$-80i$
$z(x^2-y^2)$	0	-390	$-390i$	0	-80	$80i$	0

TABLE VIII. Spin-orbit coupling parameters (meV) for the non-local part of the Hamiltonian, $H_{\text{soc}}^{\text{nlc}}$. Only elements greater than or equal to 10 meV are shown.

$h_{\uparrow\uparrow}$	Nonlocal (X_1)						
	xyz	x^3	y^3	z^3	$x(y^2-z^2)$	$y(z^2-x^2)$	$z(x^2-y^2)$
xyz	0	0	0	0	0	0	0
x^3	0	11	$-14i$	0	0	0	0
y^3	0	$14i$	0	0	0	0	0
z^3	0	0	0	0	0	0	0
$x(y^2-z^2)$	0	0	0	0	-10	0	0
$y(z^2-x^2)$	0	0	0	0	0	-12	0
$z(x^2-y^2)$	0	0	0	0	0	0	-12
$h_{\uparrow\downarrow}$	Nonlocal (X_1)						
	xyz	x^3	y^3	z^3	$x(y^2-z^2)$	$y(z^2-x^2)$	$z(x^2-y^2)$
xyz	0	0	0	0	0	0	0
x^3	0	0	0	14	0	0	0
y^3	0	0	0	$-15i$	0	0	0
z^3	0	-14	$15i$	0	0	0	0
$x(y^2-z^2)$	0	0	0	0	0	0	0
$y(z^2-x^2)$	0	0	0	0	0	0	0
$z(x^2-y^2)$	0	0	0	0	0	0	0

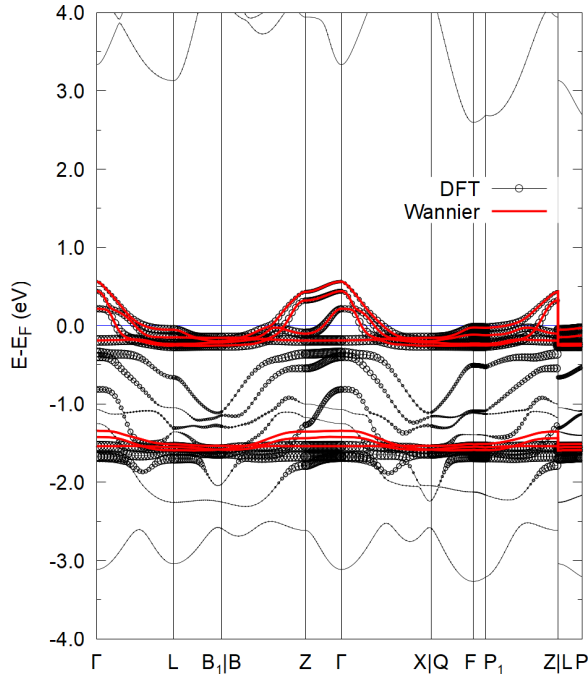


FIG. 5. Band structure of KYbSe₂ with SOC from DFT (black, circles) and from WANNIER90 (red). The size of the circles represents the Yb *f* character of the bands.

APPENDIX E: SYMMETRY IN NEAREST-NEIGHBOR BONDS

Hoppings to nearest neighbors are presented in Table IX.

TABLE IX. Nearest-neighbor hopping (meV) without spin-orbit coupling.

	X ₁ bond						
	<i>xyz</i>	<i>x</i> ³	<i>y</i> ³	<i>z</i> ³	<i>x</i> (<i>y</i> ² - <i>z</i> ²)	<i>y</i> (<i>z</i> ² - <i>x</i> ²)	<i>z</i> (<i>x</i> ² - <i>y</i> ²)
<i>xyz</i>	-3.38	-6.53	0.56	0.56	0	-0.26	0.26
<i>x</i> ³	-6.53	36.53	0.87	0.87	0	-3.94	3.94
<i>y</i> ³	0.56	0.87	80.38	-14.43	-4.96	-28.77	0.10
<i>z</i> ³	0.56	0.87	-14.43	80.38	4.96	-0.10	28.77
<i>x</i> (<i>y</i> ² - <i>z</i> ²)	0	0	-4.96	4.96	-21.23	1.07	1.07
<i>y</i> (<i>z</i> ² - <i>x</i> ²)	-0.26	-3.94	-28.77	-0.10	1.07	4.12	5.19
<i>z</i> (<i>x</i> ² - <i>y</i> ²)	0.26	3.94	0.10	28.77	1.07	5.19	4.12
	Y ₁ bond						
	<i>xyz</i>	<i>x</i> ³	<i>y</i> ³	<i>z</i> ³	<i>x</i> (<i>y</i> ² - <i>z</i> ²)	<i>y</i> (<i>z</i> ² - <i>x</i> ²)	<i>z</i> (<i>x</i> ² - <i>y</i> ²)
<i>xyz</i>	-3.38	0.56	-6.53	0.56	0.26	0	-0.26
<i>x</i> ³	0.56	80.38	0.87	-14.43	28.77	4.96	-0.10
<i>y</i> ³	-6.53	0.87	36.53	0.87	3.94	0	-3.94
<i>z</i> ³	0.56	-14.43	0.87	80.38	0.10	-4.96	-28.77
<i>x</i> (<i>y</i> ² - <i>z</i> ²)	0.26	28.77	3.94	0.10	4.12	1.07	5.19
<i>y</i> (<i>z</i> ² - <i>x</i> ²)	0	4.96	0	-4.96	1.07	-21.23	1.07
<i>z</i> (<i>x</i> ² - <i>y</i> ²)	-0.26	-0.10	-3.94	-28.77	5.19	1.07	4.12
	Z ₁ bond						
	<i>xyz</i>	<i>x</i> ³	<i>y</i> ³	<i>z</i> ³	<i>x</i> (<i>y</i> ² - <i>z</i> ²)	<i>y</i> (<i>z</i> ² - <i>x</i> ²)	<i>z</i> (<i>x</i> ² - <i>y</i> ²)
<i>xyz</i>	-3.38	0.56	0.56	-6.53	-0.26	0.26	0
<i>x</i> ³	0.56	80.38	-14.43	0.87	-28.77	0.10	-4.96
<i>y</i> ³	0.56	-14.43	80.38	0.87	-0.10	28.77	4.96
<i>z</i> ³	-6.53	0.87	0.87	36.53	-3.94	3.94	0
<i>x</i> (<i>y</i> ² - <i>z</i> ²)	-0.26	-28.77	-0.10	-3.94	4.12	5.19	1.07
<i>y</i> (<i>z</i> ² - <i>x</i> ²)	0.26	0.10	28.77	3.94	5.19	4.12	1.07
<i>z</i> (<i>x</i> ² - <i>y</i> ²)	0	-4.96	4.96	0	1.07	1.07	-21.23

- [1] E. Lieb, T. Schultz, and D. Mattis, Two soluble models of an antiferromagnetic chain, *Ann. Phys.* **16**, 407 (1961).
- [2] M. Oshikawa, Commensurability, Excitation Gap, and Topology in Quantum Many-Particle Systems on a Periodic Lattice, *Phys. Rev. Lett.* **84**, 1535 (2000).
- [3] M. B. Hastings, Lieb-Schultz-Mattis in higher dimensions, *Phys. Rev. B* **69**, 104431 (2004).
- [4] C. Broholm, R. J. Cava, S. A. Kivelson, D. G. Nocera, M. R. Norman, and T. Senthil, Quantum spin liquids, *Science* **367**, eaay0668 (2020).
- [5] P. Anderson, Resonating valence bonds: A new kind of insulator? *Mater. Res. Bull.* **8**, 153 (1973).
- [6] P. Fazekas and P. W. Anderson, On the ground state properties of the anisotropic triangular antiferromagnet, *Philos. Mag.* **30**, 423 (1974).
- [7] L. Capriotti, A. E. Trumper, and S. Sorella, Long-Range Néel Order in the Triangular Heisenberg Model, *Phys. Rev. Lett.* **82**, 3899 (1999).
- [8] Y. Zhou, K. Kanoda, and T.-K. Ng, Quantum spin liquid states, *Rev. Mod. Phys.* **89**, 025003 (2017).
- [9] Z. Zhu, P. A. Maksimov, S. R. White, and A. L. Chernyshev, Topography of Spin Liquids on a Triangular Lattice, *Phys. Rev. Lett.* **120**, 207203 (2018).
- [10] Z. Zhu and S. R. White, Spin liquid phase of the $S = \frac{1}{2}J_1 - J_2$ Heisenberg model on the triangular lattice, *Phys. Rev. B* **92**, 041105(R) (2015).
- [11] L. Ding, P. Manuel, S. Bachus, F. Grubler, P. Gegenwart, J. Singleton, R. D. Johnson, H. C. Walker, D. T. Adroja, A. D. Hillier, and A. A. Tsirlin, Gapless spin-liquid state in the structurally disorder-free triangular antiferromagnet NaYbO₂, *Phys. Rev. B* **100**, 144432 (2019).
- [12] P.-L. Dai, G. Zhang, Y. Xie, C. Duan, Y. Gao, Z. Zhu, E. Feng, Z. Tao, C.-L. Huang, H. Cao, A. Podlesnyak, G. E. Granroth, M. S. Everett, J. C. Neufeind, D. Voneshen, S. Wang, G. Tan, E. Morosan, X. Wang, H.-Q. Lin *et al.*, Spinon Fermi Surface Spin Liquid in a Triangular Lattice Antiferromagnet NaYbSe₂, *Phys. Rev. X* **11**, 021044 (2021).
- [13] B. Schmidt, J. Sichelschmidt, K. M. Ranjith, T. Doert, and M. Baenitz, Yb delafossites: Unique exchange frustration of 4*f* spin- $\frac{1}{2}$ moments on a perfect triangular lattice, *Phys. Rev. B* **103**, 214445 (2021).
- [14] Y. Shen, Y.-D. Li, H. Wo, Y. Li, S. Shen, B. Pan, Q. Wang, H. C. Walker, P. Steffens, M. Boehm, Y. Hao, D. L. Quintero-Castro, L. W. Harriger, M. D. Frontzek, L. Hao, S. Meng, Q. Zhang, G. Chen, and J. Zhao, Evidence for a spinon Fermi surface

- in a triangular-lattice quantum-spin-liquid candidate, *Nature (London)* **540**, 559 (2016).
- [15] J. A. M. Paddison, M. Daum, Z. Dun, G. Ehlers, Y. Liu, M. B. Stone, H. Zhou, and M. Mourigal, Continuous excitations of the triangular-lattice quantum spin liquid YbMgGaO_4 , *Nat. Phys.* **13**, 117 (2017).
- [16] Y. Li, D. Adroja, D. Voneshen, R. I. Bewley, Q. Zhang, A. A. Tsirlin, and P. Gegenwart, Nearest-neighbour resonating valence bonds in YbMgGaO_4 , *Nat. Commun.* **8**, 15814 (2017).
- [17] Y. Li, D. Adroja, R. I. Bewley, D. Voneshen, A. A. Tsirlin, P. Gegenwart, and Q. Zhang, Crystalline Electric-Field Randomness in the Triangular Lattice Spin-Liquid YbMgGaO_4 , *Phys. Rev. Lett.* **118**, 107202 (2017).
- [18] Z. Zhu, P. A. Maksimov, S. R. White, and A. L. Chernyshev, Disorder-Induced Mimicry of a Spin Liquid in YbMgGaO_4 , *Phys. Rev. Lett.* **119**, 157201 (2017).
- [19] I. Kimchi, A. Nahum, and T. Senthil, Valence Bonds in Random Quantum Magnets: Theory and Application to YbMgGaO_4 , *Phys. Rev. X* **8**, 031028 (2018).
- [20] W. Liu, Z. Zhang, J. Ji, Y. Liu, J. Li, X. Qang, H. Lei, G. Chen, and Q. Zhang, Rare-earth chalcogenides: A large family of triangular lattice spin liquid candidates, *Chin. Phys. Lett.* **35**, 117501 (2018).
- [21] M. Baenitz, P. Schlender, J. Sichelschmidt, Y. A. Onykiienko, Z. Zangeneh, K. M. Ranjith, R. Sarkar, L. Hozoi, H. C. Walker, J.-C. Orain, H. Yasuoka, J. van den Brink, H. H. Klauss, D. S. Inosov, and T. Doert, NaYbS_2 : A planar spin- $\frac{1}{2}$ triangular-lattice magnet and putative spin liquid, *Phys. Rev. B* **98**, 220409(R) (2018).
- [22] A. O. Scheie, E. A. Ghioldi, J. Xing, J. A. M. Paddison, N. E. Sherman, M. Dupont, L. D. Sanjeeva, S. Lee, A. J. Woods, D. Abernathy, D. M. Pajerowski, T. J. Williams, S.-S. Zhang, L. O. Manuel, A. E. Trumper, C. D. Pemmaraju, A. S. Sefat, D. S. Parker, T. P. Devereaux, R. Movshovich *et al.*, Witnessing quantum criticality and entanglement in the triangular antiferromagnet KYbSe_2 , [arXiv:2109.11527](https://arxiv.org/abs/2109.11527).
- [23] J. Xing, L. D. Sanjeeva, A. F. May, and A. S. Sefat, Synthesis and anisotropic magnetism in quantum spin liquid candidates AYbSe_2 ($A = \text{K}$ and Rb), *APL Mater.* **9**, 111104 (2021).
- [24] A. O. Scheie, Y. Kamiya, H. Zhang, S. Lee, A. J. Woods, M. G. Gonzalez, B. Bernu, J. Xing, Q. Huang, Q. M. Zhang, J. Ma, E. S. Choi, D. M. Pajerowski, H. Zhou, A. S. Sefat, L. Messio, R. Movshovich, C. D. Batista, and D. A. Tennant, Non-linear magnons and exchange Hamiltonians of delafossite proximate quantum spin liquids, [arXiv:2207.14785](https://arxiv.org/abs/2207.14785).
- [25] J. Xing, L. D. Sanjeeva, J. Kim, G. R. Stewart, M.-H. Du, F. A. Reboredo, R. Custelcean, and A. S. Sefat, Crystal synthesis and frustrated magnetism in triangular lattice CsRESe_2 ($RE = \text{La-Lu}$): Quantum spin liquid candidates CsCeSe_2 and CsYbSe_2 , *ACS Mater. Lett.* **2**, 71 (2020).
- [26] T. Xie, A. A. Eberharter, J. Xing, S. Nishimoto, M. Brando, P. Khanenko, J. Sichelschmidt, A. A. Turrini, D. G. Mazzone, P. G. Naumov, L. D. Sanjeeva, N. Harrison, A. S. Sefat, B. Normand, A. M. Lauchli, A. Podlesnyak, and S. E. Nikitin, Complete field-induced spectral response of the spin-1/2 triangular-lattice antiferromagnet CsYbSe_2 , [arXiv:2210.04928](https://arxiv.org/abs/2210.04928).
- [27] R. Iizuka, S. Michimura, R. Numakura, Y. Uwatoko, and M. Kosaka, Single crystal growth and physical properties of ytterbium sulfide KYbS_2 with triangular lattice, *JPS Conf. Proc.* **30**, 011097 (2020).
- [28] R. Sarkar, P. Schlender, V. Grinenko, E. Haeussler, P. J. Baker, T. Doert, and H.-H. Klauss, Quantum spin liquid ground state in the disorder free triangular lattice NaYbS_2 , *Phys. Rev. B* **100**, 241116(R) (2019).
- [29] K. M. Ranjith, S. Luther, T. Reimann, B. Schmidt, P. Schlender, J. Sichelschmidt, H. Yasuoka, A. M. Strydom, Y. Skourski, J. Wosnitzer, H. Kühne, T. Doert, and M. Baenitz, Anisotropic field-induced ordering in the triangular-lattice quantum spin liquid NaYbSe_2 , *Phys. Rev. B* **100**, 224417 (2019).
- [30] Z. Zhang, J. Li, M. Xie, W. Zhuo, D. T. Adroja, P. J. Baker, T. G. Perring, A. Zhang, F. Jin, J. Ji, X. Wang, J. Ma, and Q. Zhang, Low-energy spin dynamics of the quantum spin liquid candidate NaYbSe_2 , *Phys. Rev. B* **106**, 085115 (2022).
- [31] K. M. Ranjith, D. Dmytriieva, S. Khim, J. Sichelschmidt, S. Luther, D. Ehlers, H. Yasuoka, J. Wosnitzer, A. A. Tsirlin, H. Kühne, and M. Baenitz, Field-induced instability of the quantum spin liquid ground state in the $J_{\text{eff}} = \frac{1}{2}$ triangular-lattice compound NaYbO_2 , *Phys. Rev. B* **99**, 180401(R) (2019).
- [32] M. M. Bordelon, E. Kenney, C. Liu, T. Hogan, L. Posthuma, M. Kavand, Y. Lyu, M. Sherwin, N. P. Butch, C. Brown, M. J. Graf, L. Balents, and S. D. Wilson, Field-tunable quantum disordered ground state in the triangular-lattice antiferromagnet NaYbO_2 , *Nat. Phys.* **15**, 1058 (2019).
- [33] J. Xing, L. D. Sanjeeva, J. Kim, G. R. Stewart, A. Podlesnyak, and A. S. Sefat, Field-induced magnetic transition and spin fluctuations in the quantum spin-liquid candidate CsYbSe_2 , *Phys. Rev. B* **100**, 220407(R) (2019).
- [34] A. A. Kulbakov, S. M. Avdoshenko, I. Puente-Orench, M. Deeb, M. Doerr, P. Schlender, T. Doert, and D. S. Inosov, Stripe- $\gamma\gamma$ magnetic order in the triangular-lattice antiferromagnet KCeS_2 , *J. Phys.: Condens. Matter* **33**, 425802 (2021).
- [35] S. M. Avdoshenko, A. A. Kulbakov, E. Häußler, P. Schlender, T. Doert, J. Ollivier, and D. S. Inosov, Spin-wave dynamics in the KCeS_2 delafossite: A theoretical description of powder inelastic neutron-scattering data, *Phys. Rev. B* **106**, 214431 (2022).
- [36] J. G. Rau and M. J. P. Gingras, Frustration and anisotropic exchange in ytterbium magnets with edge-shared octahedra, *Phys. Rev. B* **98**, 054408 (2018).
- [37] Y. Iqbal, W.-J. Hu, R. Thomale, D. Poilblanc, and F. Becca, Spin liquid nature in the Heisenberg $J_1 - J_2$ triangular antiferromagnet, *Phys. Rev. B* **93**, 144411 (2016).
- [38] D.-V. Bauer and J. O. Fjærestad, Schwinger-boson mean-field study of the $J_1 - J_2$ Heisenberg quantum antiferromagnet on the triangular lattice, *Phys. Rev. B* **96**, 165141 (2017).
- [39] S.-S. Gong, W. Zhu, J.-X. Zhu, D. N. Sheng, and K. Yang, Global phase diagram and quantum spin liquids in a spin- $\frac{1}{2}$ triangular antiferromagnet, *Phys. Rev. B* **96**, 075116 (2017).
- [40] S. Onoda, Effective quantum pseudospin-1/2 model for Yb pyrochlore oxides, *J. Phys.: Conf. Ser.* **320**, 012065 (2011).
- [41] S. Onoda and Y. Tanaka, Quantum fluctuations in the effective pseudospin- $\frac{1}{2}$ model for magnetic pyrochlore oxides, *Phys. Rev. B* **83**, 094411 (2011).
- [42] J. G. Rau and M. J. P. Gingras, Magnitude of quantum effects in classical spin ices, *Phys. Rev. B* **92**, 144417 (2015).
- [43] J. G. Rau, S. Petit, and M. J. P. Gingras, Order by virtual crystal field fluctuations in pyrochlore XY antiferromagnets, *Phys. Rev. B* **93**, 184408 (2016).
- [44] G. Kresse and J. Furthmüller, Efficient iterative schemes for *ab initio* total-energy calculations using a plane-wave basis set, *Phys. Rev. B* **54**, 11169 (1996).

- [45] G. Kresse and J. Furthmüller, Efficiency of *ab-initio* total energy calculations for metals and semiconductors using a plane-wave basis set, *Comput. Mater. Sci.* **6**, 15 (1996).
- [46] J. P. Perdew, K. Burke, and M. Ernzerhof, Generalized Gradient Approximation Made Simple, *Phys. Rev. Lett.* **77**, 3865 (1996).
- [47] P. E. Blöchl, Projector augmented-wave method, *Phys. Rev. B* **50**, 17953 (1994).
- [48] G. Kresse and D. Joubert, From ultrasoft pseudopotentials to the projector augmented-wave method, *Phys. Rev. B* **59**, 1758 (1999).
- [49] A. A. Mostofi, J. R. Yates, G. Pizzi, Y.-S. Lee, I. Souza, D. Vanderbilt, and N. Marzari, An updated version of WANNIER90: A tool for obtaining maximally-localised Wannier functions, *Comput. Phys. Commun.* **185**, 2309 (2014).
- [50] N. Marzari and D. Vanderbilt, Maximally localized generalized Wannier functions for composite energy bands, *Phys. Rev. B* **56**, 12847 (1997).
- [51] I. Souza, N. Marzari, and D. Vanderbilt, Maximally localized Wannier functions for entangled energy bands, *Phys. Rev. B* **65**, 035109 (2001).
- [52] G.-X. Zhi, C.-C. Xu, S.-Q. Wu, F.-L. Ning, and C. Cao, WannSymm: A symmetry analysis code for Wannier orbitals, *Comput. Phys. Commun.* **271**, 108196 (2022).
- [53] J. C. Slater, *Quantum Theory of Atomic Structure*, Vol. I (McGraw-Hill, New York, 1960).
- [54] A. Meftah, J.-F. Wyart, W.-U. L. Tchang-Brillet, C. Blaess, and N. Champion, Spectrum and energy levels of Yb⁴⁺ free ion (Yb V), *Phys. Scr.* **88**, 045305 (2013).
- [55] L. Havlák, J. Fábry, M. Henriques, and M. Dušek, Structure determination of KScS₂, RbScS₂ and KLnS₂ (Ln = Nd, Sm, Tb, Dy, Ho, Er, Tm and Yb) and crystal–chemical discussion, *Acta Crystallogr., Sect. C* **71**, 623 (2015).
- [56] A. K. Gray, B. R. Martin, and P. K. Dorhout, Crystal structure of potassium ytterbium(III) selenide, KYbSe₂, *Z. Kristallogr. New Cryst. Struct.* **218**, 20 (2003).
- [57] A. K. Gray, B. R. Martin, and P. K. Dorhout, Crystal structure of sodium ytterbium(III) selenide, NaYbSe₂, *Z. Kristallogr. New Cryst. Struct.* **218**, 19 (2003).
- [58] See Supplemental Material at <http://link.aps.org/supplemental/10.1103/PhysRevResearch.5.033050> for crystal structures and tight-binding Hamiltonian files with and without spin-orbit coupling for each of the five systems.
- [59] G. Jha and T. Heine, DFTB parameters for the periodic table: Part III, spin-orbit coupling, *J. Chem. Theory Comput.* **18**, 4472 (2022).
- [60] P. A. Maksimov, Z. Zhu, S. R. White, and A. L. Chernyshev, Anisotropic-Exchange Magnets on a Triangular Lattice: Spin Waves, Accidental Degeneracies, and Dual Spin Liquids, *Phys. Rev. X* **9**, 021017 (2019); Erratum: Anisotropic-Exchange Magnets on a Triangular Lattice: Spin Waves, Accidental Degeneracies, and Dual Spin Liquids [Phys. Rev. X 9, 021017 (2019)], **12**, 019902(E) (2022).
- [61] Y. Li, P. Gegenwart, and A. A. Tsirlin, Spin liquids in geometrically perfect triangular antiferromagnets, *J. Phys.: Condens. Matter* **32**, 224004 (2020).
- [62] M. Hoffmann and S. Blügel, Systematic derivation of realistic spin models for beyond-Heisenberg solids, *Phys. Rev. B* **101**, 024418 (2020).
- [63] R. Soni, N. Kaushal, C. Şen, F. A. Reboredo, A. Moreo, and E. Dagotto, Estimation of biquadratic and bicubic Heisenberg effective couplings from multiorbital Hubbard models, *New J. Phys.* **24**, 073014 (2022).
- [64] F. Mila and F.-C. Zhang, On the origin of biquadratic exchange in spin 1 chains, *Eur. Phys. J. B* **16**, 7 (2000).
- [65] R. Pohle, N. Shannon, and Y. Motome, Spin nematics meet spin liquids: Exotic quantum phases in the spin-1 bilinear-biquadratic model with Kitaev interactions, *Phys. Rev. B* **107**, L140403 (2023).
- [66] A. Kartsev, M. Augustin, R. F. L. Evans, K. S. Novoselov, and E. J. G. Santos, Biquadratic exchange interactions in two-dimensional magnets, *npj Comput. Mater.* **6**, 150 (2020).
- [67] M. D. Jones and R. C. Albers, Spin-orbit coupling in an *f*-electron tight-binding model: Electronic properties of Th, U, and Pu, *Phys. Rev. B* **79**, 045107 (2009).